Printable dielectric elastomers of high electromechanical properties based on SEBS ink incorporated with polyphenols modified dielectric particles

Zhanxu Liu [1], Bangze Zhou [1], Chenchen Li [1], Yuhao Wang [1], Shipeng Wen[2], Yanfen Zhou [1], Liang Jiang [1, *], Fenglei Zhou [1,3], Anthony Betts [4], Stephen Jerrams [5]

[1]College of Textiles and Clothing, Qingdao University, Qingdao 266071, China

[2] Beijing Engineering Research Center of Advanced Elastomers, Beijing University of Chemical Technology, Beijing 100029, China

[3] Centre for Medical Image Computing, University College London, London, WC1V 6LJ, UK

[4] Applied Electrochemistry Group, FOCAS, Technological University Dublin (TU Dublin), City Campus, Kevin St, Dublin D08 NF82, Ireland

[5] Centre for Elastomer Research, FOCAS, Technological University Dublin (TU Dublin), City Campus, Kevin St, Dublin D08 NF82, Ireland

[*] Corresponding author, email address: liang.jiang@qdu.edu.cn (Liang Jiang)

Abstract

In this work, a recently developed 3D additive processing technology termed electrohydrodynamic (EHD) printing was employed to fabricate dielectric elastomer (DE) films by using styrene-ethylene-butylene-styrene (SEBS) inks with the addition of high dielectric titanium dioxide (TiO_2) nanoparticles. In order to improve the dispersibility of TiO_2 in the SEBS matrix, extracted walnut polyphenols were utilized for surface modification of TiO_2 nanoparticles labelled wp-TiO_2. The effect of the applied voltage on the ink jet morphology of the obtained SEBS based inks during EHD printing was analyzed. The prepared films had precision patterned shapes and their morphology was studied. It revealed that the dispersibility of TiO_2 nanoparticles in the SEBS matrix and their compatibility were greatly improved using this procedure. Furthermore, the printed DE films were found to have excellent mechanical, dielectric and electromechanical properties. For the range of DEs fabricated, the SEBS/10%wp-TiO_2 composite exhibited the maximum actuated area strain of 21.5% at an electric field of about 34.0 V/μm without degradation of other properties.

Keywords: Dielectric elastomer; Walnut polyphenols; Surface modification; EHD printing

1 Introduction

Dielectric elastomers (DEs) are a group of smart polymers which have the ability to provide highly efficient electromechanical energy conversion [1-4]. Due to the inherent advantages of low cost, large electro-induced deformation, high energy density and fast response time, DEs have potential applications for sensors, actuators and artificial muscles [5-7]. When a high electric field (E) is applied, the DE film coated with compliant electrodes expands in area and decreases in thickness because of the Maxwell stress (P) [8] generated. A DE can quickly recover its shape upon removal of a high electric field. DEs are virtually incompressible, while being excellent insulators making them ideal for small electro-deformations which obey Hooke's law. Consequently the theoretical deformation in the thickness direction conforms to equation given by [9]:

$$S_z = -\frac{\varepsilon_0 \varepsilon_r E^2}{Y} \tag{1}$$

where Y is elastic modulus, ε_0 is the permittivity of a vacuum, ε_r represents the dielectric constant of the DE. From the equation, it is evident that enhanced actuated strain can be produced by raising the dielectric constant and lowering the elastic modulus.

For increasing the dielectric constant of DEs, highly dielectric ceramic particles such as calcium copper titanate (CCTO) [10], barium titanate (BaTiO$_3$) [11], and titanium dioxide (TiO$_2$) [12] have been used as fillers incorporated into polymer matrices. However, the poor interfacial interactions between fillers and matrices often leads to a decreased dielectric strength and an increased leakage current [13, 14]. In this situation, surface modification has frequently been employed to form a functionalized interfacial layer on the surfaces of fillers to improve the compatibility between the inorganic oxide particles and DE matrices. For example, Yang et al. [15] modified TiO$_2$ particles by using poly(catechol/polyamine) (PCPA) and γ-methacryloxypropyl trimethoxy silane (KH570). The dispersion of TiO$_2$ in a natural rubber (NR) matrix was improved and the

composites produced a large actuated strain which was about 2 times larger than that of pure NR (6.0%). Dang et al. [16] fabricated a kind of DE composite by using polyurethane (PU) and 4,4'-diphenylmethane diisocyanate (MDI) modified $BaTiO_3$ (BT) particles. The PU composite containing 6 wt% BT/MDI particles had an energy-transduction density of 2.88 mJ/cm^3 at 900 V, which was 1.4 times higher than BT/PU and 3.8 times higher than PU. Polydopamine (PDA) deposition attracts an increase in interests in the surface modification of various materials due to its simplicity and high efficiency [17, 18]. However, PDA presents the problem of instability due to its quick deterioration. By contrast, polyphenols such as green tea catechins and walnut polyphenols, which have been used for surface modification [19-21], are much more stable. Moreover, they are abundant in nature [22].

Most of DE actuator (DEA) based applications are hand-made which is not only time consuming and cumbersome, but also leads to the inconsistency of material quality. In order to conquer the drawbacks, endeavors have been attempted to fabricate DEAs automatically [23-25]. However, the automated fabricating process, which is often required two or more machines to obtain DEAs, was regarded as complexity. In comparison, electrohydrodynamic (EHD) printing [26-29] is a new and versatile non-contact direct fabrication technology in which the ink is drawn along the applied electric field with the formation of a Taylor cone and a fine jet from the top of the cone [30, 31]. Hence, EHD enables the rapid design and fabrication of soft materials in numerous arbitrary geometries.

In this work, patterned DEAs were prepared by using EHD printing with SEBS as the matrix material and TiO_2 nanoparticles as the dielectric filler. SEBS was used because of its good strength, flexibility and excellent heat resistance [32-35]. Walnut polyphenols modified TiO_2 particles (wp-TiO_2) were prepared in order to improve

particle interfacial interaction with the SEBS matrix. The formation of the liquid cone and jet behavior under various voltages during EHD printing for inks with different dielectric particles' content was investigated for the sake of achieving a high printing resolution. Furthermore, the mechanical, dielectric and electromechanical properties were investigated along with the long-term working stability of the printed SEBS/TiO$_2$ and SEBS/wp-TiO$_2$ composite films with the aim to obtain DEs with enhanced electromechanical performance.

2 Experimental

2.1 Materials

SEBS (G6703-0001) was purchased from PolyOne Corporation, China. Walnut skin was bought from Xi'an Wanfang Biotechnology Co., Ltd, China. TiO$_2$ microparticles (40 nm) and ethanol were provided by Shanghai Macklin Biochemical Technology Co., Ltd. Xylene, tetrahydrofuran and n-heptane of analytical grade were purchased from Sinopharm Chemical Reagent Co., Ltd. The compliant electrode was fabricated by adding multiwall carbon nanotube in liquid silicone rubber, which is purchased from Hong Ye Jie Technology Co., Ltd, with a weight percentage of 5%.

2.2 Walnut polyphenols extraction

Walnut skin was ground into powder and added in a solution consisting of ethanol and water with a ratio of 3:5. Then the mixture was ultrasonicated at 60 ºC for 1h and subsequently centrifuged for 30 min at a speed of 5000 rev/min. The obtained supernatant was further centrifugated for 3 times. The resultant extracts were finally utilized for the surface treatment of TiO$_2$ nanoparticles.

2.3 Fabrication of wp-TiO$_2$ particles

Initially, TiO$_2$ particles were filled into the extracts and stirred at ambient temperature for 2 days. Then, the modified particles were removed from the mixture by

centrifugation and washed 3 times with ultrasonication in deionized water for 10 min. Finally, they were dried and ground into fine powders. The surface modified TiO_2 is labelled as wp-TiO_2.

2.4 Preparation of SEBS based inks

The SEBS ink with a concentration of 25 wt% was prepared by dissolving SEBS pellets in the mixture of two solvents of xylene and tetrahydrofuran at a weight ratio of 3:1, then magnetically stirred for 18 h. The SEBS/TiO_2 inks were obtained by adding different amount of TiO_2 particles into SEBS ink and magnetically stirred for 6 h. The weight percentage of TiO_2 in SEBS/TiO_2 was 10 wt%, 20 wt% and 30 wt%. The resulting SEBS/TiO_2 ink containing different amounts of TiO_2 were denoted as SEBS/10%TiO_2, SEBS/20%TiO_2, SEBS/30%TiO_2, respectively. The SEBS/wp-TiO_2 inks with various contents of wp-TiO_2 were prepared in the same way. The resulting SEBS/wp-TiO_2 inks of different wp-TiO_2 content were denoted as SEBS/10%wp-TiO_2, SEBS/20%wp-TiO_2 and SEBS/30%wp-TiO_2, respectively. The preparation process of SEBS inks is illustrated in Fig. 1.
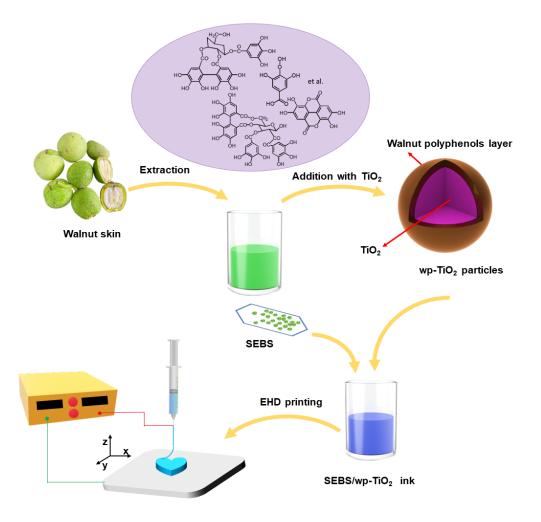
Fig. 1. Schematic illustration of the preparation of SEBS inks.

2.5 EHD printing of DE films and compliant electrode

The prepared SEBS composite ink was printed by the homemade EHD printing system which was reported in our previous work [36]. The diameter of the jet needle for printing was 400 μm and the ink flow rate was maintained at 14.7 μL/min. The distance between the needle tip and the substrate was about 5 mm. When an electric field was applied, the printing liquid was deposited on the substrate due to the electrostatic field force. The printed jet morphology is photographed by a high-speed camera. The whole process of printing is also shown in Fig. 1. For patterning compliant electrode, the electrode was loaded in syringe pump followed by adjusting the distance between the needle tip and the substrate to 2 mm. No voltage was applied during printing the

electrode.

2.6 Characterization

The chemical structures of TiO_2 and wp-TiO_2 particles were analyzed by using Fourier transform infrared (FTIR) spectroscopy (Bruker TENSOR27, Germany). Surface composition was tested by using an X-ray photoelectron spectroscopy (XPS, Thermo ESCALAB 250XI, USA). Thermal Gravimetric Analysis (TGA) of both TiO_2 and wp-TiO_2 was performed on a differential scanning calorimeter/thermogravimetric (DSC/TG) analyzer (STA 449 F3, Netzsch, Germany) from room temperature to 800 °C under N_2 atmosphere. The ink viscosity was tested by using a rotating viscosity tester (NDJ-9s, Ping Xuan scientific instrument co., Ltd., China). The jet morphology was observed by using a high-speed industrial camera (OSG030-815UM) which was purchased from Shenzhen YVSION Technology Co., Ltd, China. The width of the patterned lines was measured by using an ultra-depth 3D digital microscope (DVM6 M, Leica Microsystems Ltd., Germany). The morphologies of the samples were observed by using a scanning electron microscope (SEM) (Hitachi S-4800, Japan). Tensile tests for the DE composite films obtained were performed by employing an Instron 5965 tensile apparatus (Instron, Glenview, USA). Rectangular specimens having a gauge length of 40 mm and gauge width of 10 mm were used. The crosshead speed was 100 mm·min^{-1}. The dielectric constant was measured by using an Impedance Analyzer (E4990A, KEYSIGHT, China) in the frequency range from 20 Hz to 20 MHz. The actuated area strain was measured by using a home-made electromechanical testing system. This test was carried out by using DE films with original diameters of 60 mm and thicknesses of around 0.3 mm at ambient temperature. The applied voltage was increased by 200 V every 3 s.

3 Results and Discussion

3.1 Surface modification of TiO$_2$ particles

Fig. 2 (a) shows the FTIR spectrum of TiO$_2$ and wp-TiO$_2$ particles. It can be seen that the spectrum of wp-TiO$_2$ had a strong peak at 3380 cm^{-1}, which was assigned to the -OH stretching vibrations arising from the presence of walnut polyphenols. The lower intensity peaks at 3380 cm^{-1} that appeared in the spectrum of TiO$_2$ were mainly caused by residual water or possibly residual surface hydroxide species on the TiO$_2$ surface. The peak at 1260 cm^{-1} belonged to the -C-O stretching vibration. A strong absorption peak at 1635 cm^{-1} indicated the carbonyl C=O stretching vibrations probably resulting from walnut polyphenols' self-polymerization.

TGA was performed to determine the thermal decomposition of TiO$_2$ and wp-TiO$_2$ nanoparticles. Fig. 2 (b) shows that the total weight loss at temperatures ranging from 40 °C to 800 °C for TiO$_2$ and wp-TiO$_2$ nanoparticles was 2.09% and 7.23%, respectively. The reduction in weight for wp-TiO$_2$ particles in the whole temperature range was attributed to dehydration from the -OH bonds incorporated in the lattice and the elimination of CO$_2$ from the contaminated TiO$_2$ [4]. The weight loss of wp-TiO$_2$ nanoparticles was 5.14% larger than that of TiO$_2$ nanoparticles, confirming the existence of the polyphenol outer layer.
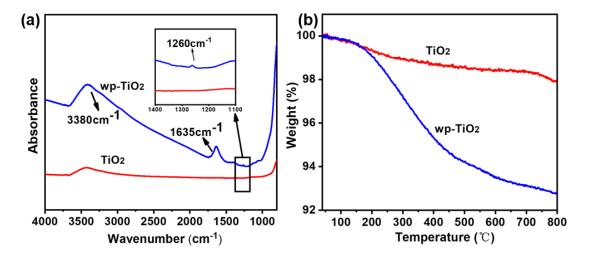

Fig. 2. (a) FTIR spectrum and (b)TG curves for TiO$_2$ and wp-TiO$_2$ particles.

Fig. 3 (a) and (c) presents the XPS wide-range scan spectrum of TiO_2 particles and wp-TiO_2 particles respectively. The carbon peak at 284.6 eV can be attributed to some carbon contamination. Fig. 3 (b) and (d) show the O 1s core level spectra of TiO_2 and wp-TiO_2 nanoparticles, respectively. The peak at 531 eV was ascribed to the presence of -OH groups while that at 533.01 eV indicated the existence of -C=O groups [15]. The amount of -OH and -C=O groups for TiO_2 particles was 28.69% and 5.84% respectively, while these contents increased to 35.52% and 19.73% for the wp-TiO_2 nanoparticles. The enhancement of the levels of both hydroxyl and carbonyl groups indicates the successful deposition of walnut polyphenols on the surface of the TiO_2 nanoparticles.
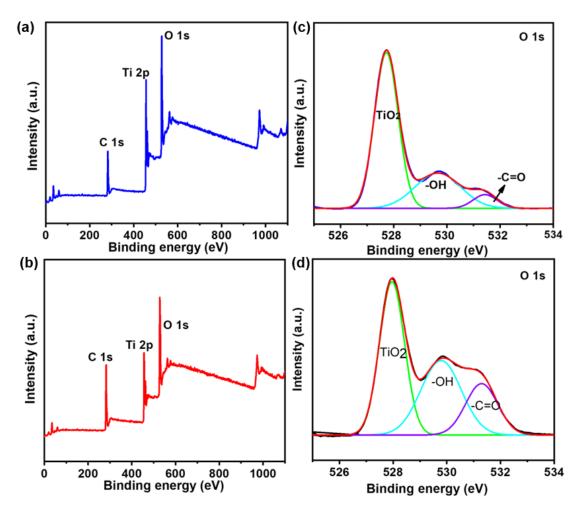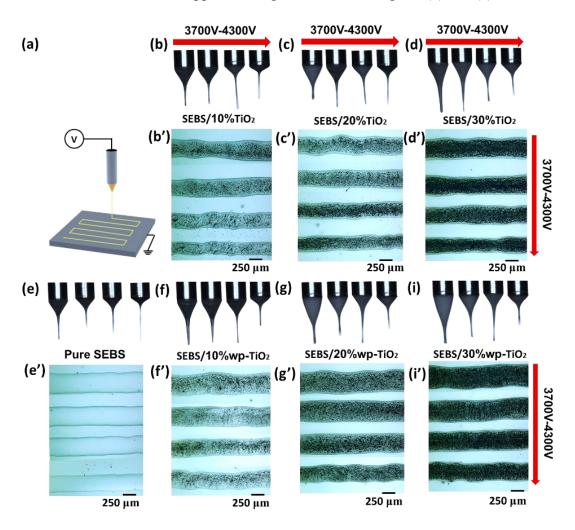

Fig. 3. XPS wide scan of (a) TiO_2 particles and (b) wp-TiO_2 particles; O 1s core level spectra of (c) TiO_2 particles and (d) wp-TiO_2 particles.

3.2 EHD printing of SEBS/TiO₂ composites

The cone angle θ is a significant parameter of EHD printing which is affected by many factors including electric field force, viscous force, surface tension and air pressure, as shown in Fig. S1 (f). Fig. 4 (b-i) shows the ink jet morphology of all inks used in this work. As can be seen from the figure, the cone angle θ rose with increasing voltage at a constant ink feed rate. This occurs because when the liquid supply rate remained constant, the high electrostatic field force, generated by the high voltage accelerated the speed of the jet launched from the nozzle, causing an increase in cone angle [23]. The relationship between cone angle θ and voltage is showed in Fig. S1 (a) and (b).

The widths of the patterned lines were used to evaluate the printing resolution (shown in Fig.4 (a)) performed. Fig. 4 (b'-i') shows the morphology of patterned lines obtained under varied high voltages and contents of TiO₂ particles. For each specification of SEBS printing inks, the patterned line width gradually abated with increasing voltage. The main reason for this is that the force from the increased electric field accelerated the jet velocity when the applied voltage was increased. Therefore, under the condition of constant liquid supply velocity, the cone volume decreased and the jet diameter became thinner with increasing voltage, which resulted in diminished line width [37]. Moreover, it was found that the patterned line width was uneven for each ink formulation at the voltage of 3700 V. It is probably ascribed to an insufficient electric field force produced by the low voltage, finally caused an unstable jet [38]. This in turn resulted in an unstable printing. As the voltage increased to 3900-4100 V, the printed line width was even and smooth. When the voltage was up to or beyond 4300 V, the jet became unstable and the line width became uneven again. Thus, 4100 V was determined to be the optimum applied voltage in order to obtain a uniform and high-resolution line width. Furthermore, the line width of SEBS/wp-TiO₂ ink was wider than that of

SEBS/TiO$_2$ ink at the same applied voltages as shown in Fig. S1 (d) and (e).

Fig. 4. (a) Schematic diagram of patterned line width by using EHD printing; (b-i) Jet behavior of the ink by different types of SEBS inks under various voltages; (b'-i') The morphology of patterned lines obtained under varied high voltages and contents of TiO$_2$ particles.

Fig. 5 (a-f) shows the surface morphology of the printed SEBS/TiO$_2$ and SEBS/wp-TiO$_2$ composites. It can be seen that many agglomerates of TiO$_2$ nanoparticles were observed on the surfaces of SEBS/TiO$_2$ composites. Both the number and the size of the agglomerates increased with increasing TiO$_2$ content. This indicates poor dispersibility of the TiO$_2$ nanoparticles in the SEBS matrices. It can also be seen that the agglomerates in the SEBS/10%wp-TiO$_2$ composite, the SEBS/20%wp-TiO$_2$

composite and the SEBS/30%wp-TiO$_2$ composite were smaller than those of the SEBS composites at comparable particle contents. Compared with the SEBS/TiO$_2$ composites, the SEBS/wp-TiO$_2$ composites exhibited significantly improved filler dispersibility with fewer agglomerates. In addition, the interfaces between the SEBS and the wp-TiO$_2$ nanoparticles were more indistinct than those of the composites filled with pristine TiO$_2$ particles. It is feasible that walnut polyphenols which contain a large amount of hydroxyl groups coated on to the surface of TiO$_2$ nanoparticles provided more active sites for hydrogen bond formation between the TiO$_2$ and the SEBS ink to produce enhanced molecular interactions. Ultimately this leads to an improved adhesion or compatibility between the wp-TiO$_2$ and SEBS.
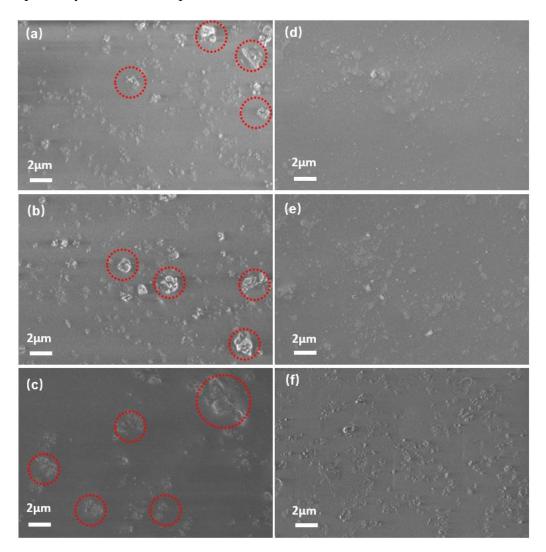

Fig. 5. SEM image of (a) SEBS/10%TiO$_2$, (b) SEBS/20%TiO$_2$, (c) SEBS/30%TiO$_2$,

(d) SEBS/10%wp-TiO$_2$, (e) SEBS/20%wp-TiO$_2$ (f) SEBS/30%wp-TiO$_2$.

3.3 Mechanical properties

The mechanical properties of the SEBS/TiO$_2$ and the SEBS/wp-TiO$_2$ composites are shown in Fig. 6. Fig. 6 (a) and (b) show typical stress-strain curves for SEBS/TiO$_2$ and SEBS/wp-TiO$_2$ composites respectively, while the average value of tensile strength and elongation at break is presented in Fig. 6 (c). It can be seen that the tensile strength of both SEBS/TiO$_2$ and SEBS/wp-TiO$_2$ composites was larger than that of pure SEBS due to the reinforcement of TiO$_2$ and wp-TiO$_2$ nanoparticles in the SEBS matrices. The ultimate tensile strength of all SEBS based DEs was below 1 MPa. The SEBS/30%wp-TiO$_2$ composite exhibited the maximum tensile strength of 0.64 MPa, which was 0.27 MPa higher than the pure SEBS. The SEBS/10%wp-TiO$_2$ composite possessed the highest elongation among these composite materials, probably because the small amount of inorganic filler did not have sufficiently strong reinforcement between the molecules [39]. Thus, it did little to hinder the elongation of long-chain molecules during stretching and hence the molecular chains were prone to slippage when subjected to external forces. Nevertheless, the elongation at break for the SEBS/wp-TiO$_2$ printed composites was above 1700%, which is beneficial for DEs to achieve large actuated area strains.

As shown in Fig. 6 (c), for the same particle content, the tensile strength of SEBS/wp-TiO$_2$ was higher than that of SEBS/TiO$_2$ because of the improved particle dispersion and enhanced interfacial interaction between the organic SEBS and inorganic TiO$_2$ in the SEBS/wp-TiO$_2$ composites [40]. However, the elongation at break of both SEBS/TiO$_2$ and the SEBS/wp-TiO$_2$ was reduced with the increase in filler content although the SEBS/wp-TiO$_2$ composites exhibited higher elongations than the corresponding SEBS/TiO$_2$ composites. The reductions in elongation at break is

probably due to TiO$_2$ or wp-TiO$_2$ particles in the SEBS composite being stiffer, causing a reinforcing effect. In this situation, hindered mobility of polymer chains brought about the decrease in elongation at break [41].
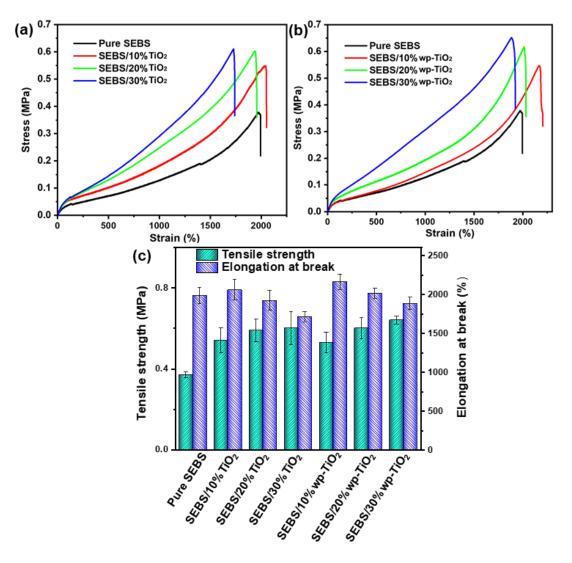

Fig. 6. Stress-strain curves of (a) SEBS/TiO$_2$ and (b) SEBS/wp-TiO$_2$ composites; (c) Histogram of tensile strength and elongation at break of SEBS composites.

3.4 Electromechanical properties

Fig. 7 exhibits the dielectric properties of SEBS/TiO$_2$ and SEBS/wp-TiO$_2$ composites over a wide frequency range. As shown in Fig. 7 (a) and (c), the dielectric constant for each printed film decreased with increasing frequency, most probably due to dipole polarization and interfacial polarization [42]. The pure SEBS showed the lowest

dielectric constant of 2.8 at 1 kHz which was largely independent of frequency although it increased below 1 kHz, as did the curves containing the filler materials. Compared with the SEBS/TiO$_2$ composites, the SEBS/wp-TiO$_2$ composites displayed a higher dielectric constant for identical particle contents. The increase in dielectric constant could have occurred because polyphenols improved the dispersion of TiO$_2$ particles in the SEBS matrix resulting in more interfacial polarization between them [43]. In addition, more charges may well have accumulated on the surface of the wp-TiO$_2$ nanoparticles allowing formation of micro-capacitors, which was beneficial for increasing the dielectric constant [15].

Fig. 7 (b) and (d) shows the dielectric loss tangent of SEBS/TiO$_2$ and SEBS/wp-TiO$_2$ composites as a function of frequency. As indicated in these figures, the dielectric loss tangent of both SEBS/TiO$_2$ and SEBS/wp-TiO$_2$ decreased monotonically with increasing frequency, although it was less pronounced in the case of the SEBS/wp-TiO$_2$. This was probably because the enhanced interfacial interactions between the particles and the matrix may have restricted the polymer chains' mobility and the dipole polarization of the SEBS composite. For the same particle content, the dielectric loss tangent at 1 kHz of SEBS/wp-TiO$_2$ composite was lower than that of the SEBS/TiO$_2$ composites. It is mainly due to that the walnut polyphenols' surface modification of TiO$_2$ nanoparticles limited the migration and accumulation of space charge and hence resulted in a low leakage current [44].
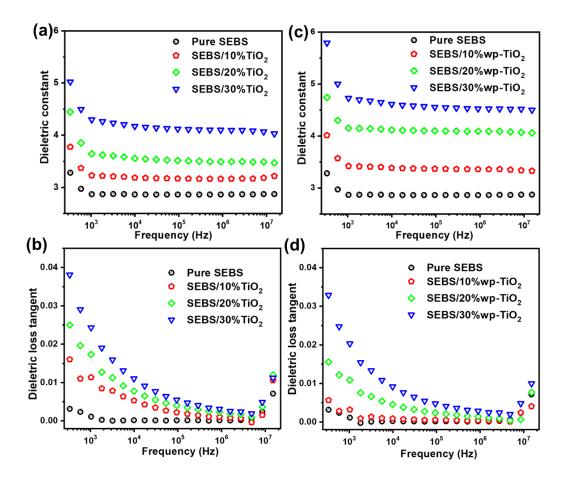
Fig. 7. Dielectric constant versus frequency for (a) SEBS/TiO$_2$ and (c) SEBS/wp-TiO$_2$ composites; Dielectric loss tangent versus frequency for (b) SEBS/TiO$_2$ and (d) SEBS/wp-TiO$_2$ composites.

Fig. 8 (a) shows the working principle of DEs. As described previously, when an external electric field is applied to the compliant electrode, opposite charges are generated on the top and bottom surfaces of the material and the DEs with opposite charges attract. This results in a shrinkage in thickness and an expansion in area. Photographs of the electrode coated DEs were captured by using a high-speed camera and the real-time area size of the electrode was measured using LabVIEW software. The area strain (S_a) was calculated by employing Equation (2):

$$S_a = \frac{A_1 - A_0}{A_0} \times 100\% \tag{2}$$

where A_0 and A_1 is the initial area and the actuated area of the electrode, respectively.

Fig. 8 (b) and (c) shows the dependence of actuated area strain on applied electric field for SEBS/TiO$_2$ and SEBS/wp-TiO$_2$ respectively. It can be observed that for both SEBS/TiO$_2$ and SEBS/wp-TiO$_2$ composites, the actuated area strain rised with increasing electrical field till the breakdown phenomenon occurred. For the SEBS/TiO$_2$ composites, the actuated area strain decreased gradually with increasing particle content. The probable reason for this was that the increased content of TiO$_2$ particles gave rise to an increase in the modulus of the composite (as denoted in Table S1), which then in turn led to a decrease in electromechanical sensitivity (β) [45]. Among these fabricated DE materials, the SEBS/10%wp-TiO$_2$ composite had the largest actuated area strain of 21.5% at a breakdown electric field of about 34.0 V/μm, while the largest actuated area strain of SEBS/10%TiO$_2$ was 18.9% when the applied electric field was 38.4 V/μm. By comparison with SEBS/TiO$_2$, the maximum actuated area strain for SEBS/wp-TiO$_2$ was larger for the same filler content. This is mainly attributed to wp-TiO$_2$ having a more even distribution in the SEBS matrix through introduction of the polyphenols onto the TiO$_2$ particles with a concomitant reduction of agglomerates. This in turn is beneficial for the enhancement of breakdown voltage. Moreover, in order to achieve a constant actuated strain, the applied electric field for SEBS/wp-TiO$_2$ composites was lower than that of the SEBS/TiO$_2$ composites. For example, the applied electric field for pure SEBS to achieve a field-induced area strain of 10% was approximately 35.1 V/μm, while it was 22.9 V/μm for the SEBS/20%TiO$_2$ composite and even lower at only 20.4 V/μm for the SEBS/wp-TiO$_2$ composite. This was primarily because the electromechanical sensitivity, which was representative of electromechanical properties of SEBS/wp-TiO$_2$, was higher than that of SEBS/TiO$_2$ at the same filler content.
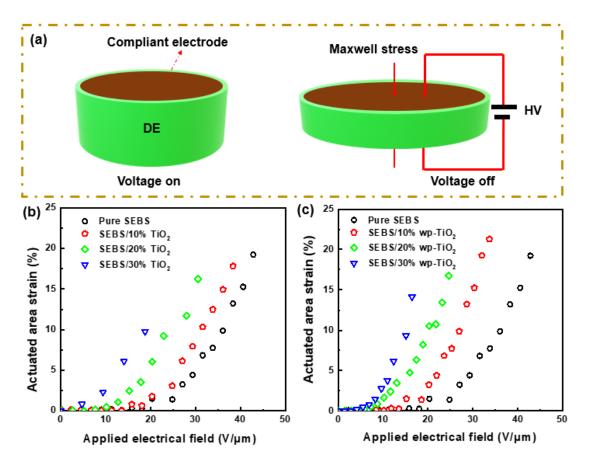
Fig. 8. (a) Schematic illustration of a dielectric elastomer before and after the application of high voltage across the film; The dependence of actuated area strain on applied electric field for (b) SEBS/TiO$_2$ composites and (c) SEBS/wp-TiO$_2$ composites.

The EHD printing technology have the capability of fabricating films with various shapes. In this work, DE films with different shapes (shown in Fig. S2) and electrode layers (shown in Fig. 9) were obtained respectively by using EHD printing. As can be seen from these figures, the patterned shapes have clear profiles. Especially, DEs with patterned electrodes including circle shape, heart shape, flower shape and T-shirt shape produced large area strains of around 20.0% under the electric field of 28.0 V/μm with the prestretch ratio of 1.6. Furthermore, the DEs exhibited an excellent actuation repeatability with the exemplification of DE patterned heart shaped electrode as shown in video S1.
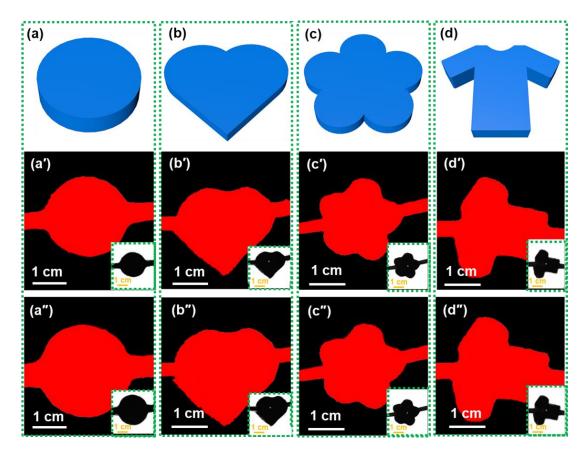
Fig. 9. 3D shapes of electrode layers patterned on DE films: (a) circle; (b) heart; (c) flower; (d) T-shirt, and their figures in LabVIEW software without ((a′), (b′), (c′), (d′)) and with applied electrical field of about 28.0 V/μm ((a″), (b″), (c″), (d″)) (the inserts are the corresponding DE films coated with compliant electrodes).

The dynamic electromechanical test for of the SEBS composites based DEs was performed by applying 200 cycles of electric field loading from 0 to 28.0 V/μm with a stepped voltage of 400 V per 3 s. Fig. 10 shows that all the SEBS composites displayed good dynamic electromechanical stability. For each sample, the largest actuated area strain achieved in consecutive loading cycles changed minimally. The largest actuated area strain in the first cycle was about 0.4% lower than that in the last cycle. The main reason for the minute change is the occurrence of an enhanced energy loss caused by a small amount of hysteresis during compression in thickness under the electrostatic force. When the applied electric field was 28.0 V/μm, the SEBS/wp-TiO$_2$ composites

exhibited the largest actuated area strain of about 11.3%, while the SEBS/10%TiO$_2$

exhibited approximately 9.8% actuated area strain and pure SEBS presented the

minimum actuated area strain of about 6.0%. This phenomenon also indicates that the

introduction of polyphenols improved the polarization performance at the interfaces

between the TiO$_2$ nanoparticles and the SEBS matrix, which gave the benefit of
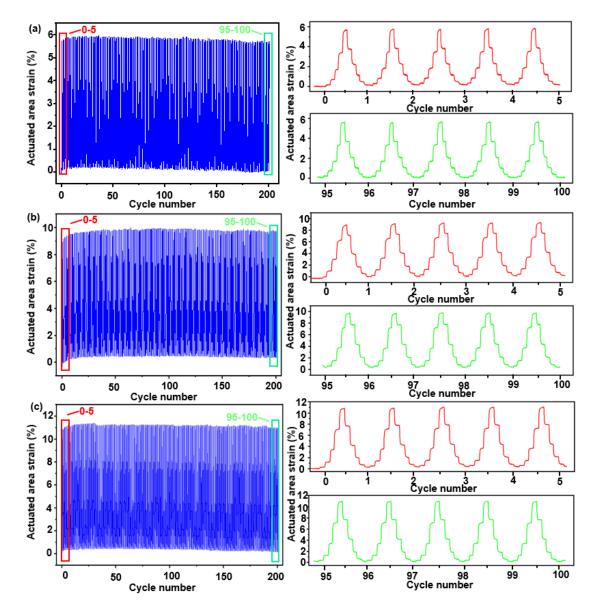
increasing the actuated area strain.

Fig. 10. The change of area strain with cycles for (a) pure SEBS; (b) SEBS/10%TiO$_2$

and (c) SEBS/10%wp-TiO$_2$ under cyclic electric field loading from 0 to 28.0 V/μm.

4 Conclusion

The EHD printing technology was employed in this work to fabricate DE composites taking advantage of a saving in materials and introducing a flexible design. An optimum working voltage of 4100 V for EHD printing was determined in order to obtain good printing resolution during fabrication of DE composites. The TiO_2 nanoparticles modified by walnut polyphenols extracted from walnut skin improved the dispersion of the SEBS composite materials due to the presence of the hydroxyl (-OH) groups, which also improved the electromechanical properties of the composite. It was found that modified SEBS/wp-TiO_2 composites showed an enhanced tensile strength compared with unmodified SEBS/TiO_2 composites. Additionally, by comparison with SEBS/TiO_2 composites, the SEBS/wp-TiO_2 composites exhibited a higher dielectric constant and a lower dielectric loss because of enhanced interfacial interactions. The SEBS/10%wp-TiO_2 composite possessing a large electromechanical sensitivity, achieved the largest actuated strain of approximately 21.5% under an electric field of 34.0 V/μm. Thus, SEBS/wp-TiO_2 composites with flexible shape design have the potential to be used for DE applications with improved electromechanical properties. As the printing process took a relatively long time to shape the material, future work will focus on shortening the printing time by using multi-needles in the EHD printing process.

Conflict of interest

The authors declare no conflict of interest.

References

[1] M. Tian, Y. Yao , S. Liu , D. Yang , L. Zhang, T. Nishi, N. Ning, Separated-structured all-organic dielectric elastomer with large actuation strain under ultralow-voltage and high mechanical strength, 3(4) (2015) 34.

[2] B. Chen, J. Lu, C. Yang, J. Yang, J. Zhou, Y. Chen, Z. Suo, Highly stretchable and transparent ionogels as nonvolatile conductors for dielectric elastomer transducers, ACS Appl Mater Interfaces 6(10) (2014) 7840-5.

[3] G.Yin, Y. Song, F Song, C Renard, Z Dang, C Shi, D. Wang, Dielectric Elastomer Generator with Improved Energy Density and Conversion Efficiency Based on Polyurethane Composites, ACS Appl Mater Interfaces 9(6) (2017) 30.

[4] M. Panahi-Sarmad, E. Chehrazi, M. Noroozi, M. Raef, M. Razzaghi-Kashani, M. Baian, Tuning the Surface Chemistry of Graphene Oxide for Enhanced Dielectric and Actuated Performance of Silicone Rubber Composites. ACS Applied Electronic Materials 1(2) (2019) 12.

[5] B. Huang, M. Li, T. Mei, D. McCoul, S. Qin, Z. Zhao, J. Zhao, Wearable Stretch Sensors for Motion Measurement of the Wrist Joint Based on Dielectric Elastomers, Sensors (Basel) 17(12) (2017) 12.

[6] P. Brochu, Q. Pei, Advances in dielectric elastomers for actuators and artificial muscles, Macromol Rapid Commun 31(1) (2010) 10-36.

[7] X. Yang, L. Sun, C. Zhang, B. Huang, Y. Chu, B. Zhan, Modulating the sensing behaviors of poly(styrene-ethylene-butylene-styrene)/carbon nanotubes with low-

dimensional fillers for large deformation sensors, Composites Part B: Engineering 160 (2019) 10.

[8] M. Fathalilou, P. Rezaei-Abajelou, A. Vefaghi, G. Rezazadeh, Dielectric Elastomer as a New Material for Electrostatically Actuated Microbeams: Stability Analysis, International Journal of Applied Mechanics 11(10) (2020) 21.

[9] W. Hu, S. Zhang, X. Niu, C. Liu, Q. Pei, An aluminum nanoparticle–acrylate copolymer nanocomposite as a dielectric elastomer with a high dielectric constant, Journal of Materials Chemistry C 2(9) (2014) 9.

[10] Y. Zhang, Y. Min, G. Wang, Z. Wang, J. Liu, Z. Luo, M. Zhang, Design and properties of calcium copper titanate/poly(dimethyl siloxane) dielectric elastomer composites, Rare Metals (2019) 6.

[11] H. Tang, Z. Zhou, H.A. Sodano, Relationship between BaTiO3 Nanowire Aspect Ratio and the Dielectric Permittivity of Nanocomposites, Acs Applied Materials & Interfaces 6(8) (2014) 5450.

[12] T. Chen, J. Qiu, K. Zhu, J. Li, Electro-mechanical performance of polyurethane dielectric elastomer flexible micro-actuator composite modified with titanium dioxide-graphene hybrid fillers, materials & design 90 (2015.11) 28.

[13] D. Zhou, Z. Ji, X. Jiang, D.R. Dunphy, J. Brinker, A. Keller, Influence of material properties on TiO2 nanoparticle agglomeration, PLoS One 8(11) (2013) 7.

[14] H. Wang, H. Kong, J. Zheng, H. Peng, C. Cao, Y. Qi, K. Fang, W. Chen, Systematically Exploring Molecular Aggregation and Its Impact on Surface Tension and Viscosity in High Concentration Solutions, Molecules 25(7) (2020) 9.

[15] D. Yang, Y. Ni, X. Kong, H. Xue, W. Guo, L. Zhang, Enhanced electromechanical properties of natural rubber using highly efficient and cost-effective mussel-inspired modification of TiO2 nanoparticles, Applied Surface Science 495 (2019) 10.

[16] Y. Yanga, Z Gao, M. Yang, M. Zheng, D. Wang, J. Zha, Y. Wen, Z. Dang, Enhanced energy conversion efficiency in the surface modified BaTiO3 nanoparticles/polyurethane nanocomposites for potential dielectric elastomer generators, Nano Energy 59 (2019) 24.

[17] J. Liang, D. Kennedy, S. Jerrams, A. Betts, Enhancement of dielectric properties with the addition of bromine and dopamine modified barium titanate particles to silicone rubber, Mrs Communications 6(4) (2016) 5.

[18] Y. Zhou, L. Li, W. Li, S. Wen, L. Jiang, S. Jerrams, J. Ma, S. Chen, The fabrication and properties of magnetorheological elastomers employing bio-inspired dopamine modified carbonyl iron particles, Smart Materials and Structures 29(5) (2020).

[19] W. Qiu, Q. Zhong, Y. Du, Y. Lv. Enzyme-triggered coatings of tea catechins/chitosan for nanofiltration membranes with high performance, Green Chemistry 18(23) (2016).

[20] S. Haddadi, T. Kohlan, S. Momeni, S. Ramazani, M. Mahdavian, Synthesis and application of mesoporous carbon nanospheres containing walnut extract for fabrication of active protective epoxy coatings, Progress in Organic Coatings 133 (2019) 14.

[21] L. Jiang, Y. Wang, S. Wen, Y. Zhou, S. Jerrams, Fabrication of dielectric elastomers with improved electromechanical properties using silicone rubber and walnut

polyphenols modified dielectric particles, Materials & design 192 (2020) 27.

[22] Wen. Qiu, H. Yang, Z. Xu, Dopamine-assisted co-deposition: An emerging and promising strategy for surface modification, Advances in Colloid & Interface Science 256 (2018) 15.

[23] M. Onses, E. Sutanto, P. Ferreira, A. Alleyne, J. Rogers, Mechanisms, Capabilities, and Applications of High-Resolution Electrohydrodynamic Jet Printing, Small 11(34) (2015) 30.

[24] M. Vaezi, H. Seitz, S. Yang, A review on 3D micro-additive manufacturing technologies, The International Journal of Advanced Manufacturing Technology 67(5-8) (2012) 1721-1754.

[25] J. Park, Y. Kang, H. Yoon, N. Park, Y. Jo, S. Jeong, J. Won, Y. Kim, Viscoelastic properties of a 3D-Printable high-dielectric paste with surface-modified BaTiO3, Composites Science and Technology 159 (2018) 7.

[26] Y. Han, J. Dong, Electrohydrodynamic (EHD) Printing of Molten Metal Ink for Flexible and Stretchable Conductor with Self-Healing Capability, Advanced Materials Technologies 3(3) (2018) 8.

[27] A. Najjaran, R. Ebrahimi, M. Rahmanpoor, Numerical Simulation of Electrohydrodynamic (EHD) Atomization in the Cone-Jet Mode, Applied Mechanics and Materials 325-326 (2013) 6.

[28] K. Zhao, D. Wang, Z. Wang, C. Jiang, Z. Abbas, Y. Zheng, Q. Yang, B. Tang, T. Liu, F. Tao, W. Xu, J. Liang, Fabrication of piezoelectric thick-film stator using electrohydrodynamic jet printing for micro rotary ultrasonic motors, Ceramics

International 46(16) (2020) 26129-26135.

[29] G. Zhang, H. Lan, L. Qian, J. Zhao, F. Wang, A Microscale 3D Printing Based on the Electric-Field-Driven Jet, 3D Printing and Additive Manufacturing 7(1) (2020) 8.

[30] A. Lee, H. Jin, H.W. Dang, K.H. Choi, K.H. Ahn, Optimization of experimental parameters to determine the jetting regimes in electrohydrodynamic printing, Langmuir 29(44) (2013) 10.

[31] Z. Xu, H. Zou, J. Wang, M.. Zhang, D. Wang, J. Liu, Fabrication of electrochemical carbon-based microelectrodes using electrohydrodynamic jet printing technique, Microsystem Technologies 24(2) (2017) 1207-1212.

[32] Y. Zhang, J. Zhang, G. Wang, Z. Wang, Z. Luo, M. Zhang. Zhang, Manufacturing and characterizing of CCTO/SEBS dielectric elastomer as capacitive strain sensors, Rare Metals (2019) 6.

[33] X. Wang, S. Pang, J. Yang, F. Yang, Structure and properties of SEBS/PP/OMMT nanocomposites, Transactions of Nonferrous Metals Society of China 16 (2006) 5.

[34] N. Calisi, A. Giuliani, M. Alderighi, J.M. Schnorr, T. Swager, F. Francesco, A. Pucci, Factors affecting the dispersion of MWCNTs in electrically conducting SEBS nanocomposites, European Polymer Journal 49(6) (2013) 1471-1478.

[35] R. Teruel-Juanes, B. Pascual-Jose, C. del Río, O. García, A. Ribes-Greus, Dielectric analysis of photocrosslinked and post-sulfonated styrene-ethylene-butylene-styrene block copolymer based membranes, Reactive and Functional Polymers 155 (2020).

[36] Y. Wang, Y. Zhou, W. Li, Z. Liu, B. Zhou, S. Wen, L. Jiang, S. Chen, J. Ma, A.

Betts, S. Jerrams and F. Zhou, The 3D printing of dielectric elastomer films assisted by electrostatic force, Smart Materials and Structures 2(30) (2020) 10.

[37] D. Wang, X. Zhao, Y. Lin, J. Liang, T. Ren, Z. Liu, J. Li, Nanoscale coaxial focused electrohydrodynamic jet printing, Nanoscale 10(21) (2018) 9867-9879.

[38] M. Yu, K. Ahn, S. Lee, Design optimization of ink in electrohydrodynamic jet printing: Effect of viscoelasticity on the formation of Taylor cone jet, 89(2016) (2015) 109-115.

[39] L. Liu, W. Zhang, N. Ning, L. Zhang, A self-healing dielectric supramolecular elastomer modified by TiO2/urea particles, Chemical Engineering Journal 375 (2019) 121933.

[40] D. Yang, S. Huang, M. Ruan, S. Li, Y. Wu, W. Guo, L. Zhang, Improved electromechanical properties of silicone dielectric elastomer composites by tuning molecular flexibility, Composites Science and Technology 155 (2018) 160-168.

[41] W. Lei, R. Wang, D. Yang, G. Hou, X. Zhou, H. Qiao, W. Wang, M. Tian, L. Zhang. Design and preparation of bio-based dielectric elastomer with polar and plasticized side chains, Rsc Advances 5(59) (2015) 47429-47438.

[42] Z. Dang, H. Xu, H. Wang, Significantly enhanced low-frequency dielectric permittivity in the BaTiO3/poly(vinylidene fluoride) nanocomposite, Applied Physics Letters 90(1) (2007) 3804.

[43] M. Ruan, D. Yang, W. Guo, S. Huang, Y. Wu, H. Wang, H. Wang, L. Zhang, Improved electromechanical properties of brominated butyl rubber filled with modified barium titanate, RSC Advances 7(59) (2017) 10.

[44] L. Xie, X. Huang, P. Jiang, Low loss and high dielectric constant poly(methyl methacrylate)BaTiO3 nanocomposites prepared by in situ atom transfer radical polymerization., International Symposium on Electrical Insulating Materials (ISEIM) (2011) 3.

[45] D.Yang, F. Ge, M. Tian, N. Ning, L. Zhang, C. Zhao, I. Kohzo, N. Toshio, H. Wang, Y. Luan, Dielectric elastomer actuator with excellent electromechanical performance using slide-ring materials/barium titanate composites, Journal of Materials Chemistry A 3(18) (2015) 9468-9479.